



HAL
open science

Impact of Antigen Density on Recognition by Monoclonal Antibodies

Laure Bar, Jérôme Dejeu, Rémy Lartia, Fouzia Bano, Ralf Richter, Liliane Coche-Guérente, Didier Boturyn

► **To cite this version:**

Laure Bar, Jérôme Dejeu, Rémy Lartia, Fouzia Bano, Ralf Richter, et al.. Impact of Antigen Density on Recognition by Monoclonal Antibodies. *Analytical Chemistry*, 2020, 92 (7), pp.5396-5403. 10.1021/acs.analchem.0c00092 . hal-02565754

HAL Id: hal-02565754

<https://hal.science/hal-02565754>

Submitted on 18 Sep 2020

HAL is a multi-disciplinary open access archive for the deposit and dissemination of scientific research documents, whether they are published or not. The documents may come from teaching and research institutions in France or abroad, or from public or private research centers.

L'archive ouverte pluridisciplinaire **HAL**, est destinée au dépôt et à la diffusion de documents scientifiques de niveau recherche, publiés ou non, émanant des établissements d'enseignement et de recherche français ou étrangers, des laboratoires publics ou privés.

Impact of antigen density on recognition by monoclonal antibodies

Laure Bar,[†] Jérôme Dejeu,[†] Rémy Lartia,[†] Fouzia Bano,[‡] Ralf P. Richter,[‡] Liliane Coche-Guérente*^{*,†} and Didier Boturyn*^{*,†}

[†]Univ. Grenoble-Alpes, CNRS, DCM UMR 5250, 570 rue de la chimie, CS 40700, 38058 Grenoble Cedex 9, France.

Email: didier.boturyn@univ-grenoble-alpes.fr

[‡]University of Leeds, School of Biomedical Sciences, Faculty of Biological Sciences, School of Physics and Astronomy, Faculty of Engineering and Physical Sciences, Astbury Center for Structural Molecular Biology, and Bragg Centre for Materials Research, Leeds, United Kingdom

ABSTRACT: Understanding antigen-antibody interactions is important to many emerging medical and bioanalytical applications. In particular, the levels of antigen expression at the cell surface may determine antibody-mediated cell death. This parameter has a clear effect on outcome in patients undergoing immunotherapy. In this context, CD20 which is expressed in the membrane of B cells has received significant attention as target for immunotherapy of leukemia and lymphoma using the monoclonal antibody rituximab. To systematically study the impact of CD20 density on antibody recognition, we designed self-assembled monolayers that display tunable CD20 epitope densities. For this purpose, we developed in situ click chemistry to functionalize SPR sensor chips. We find that the rituximab binding affinity depends sensitively and non-monotonously on CD20 surface density. Strongest binding, with an equilibrium dissociation constant ($K_D = 32$ nM) close to values previously reported from in vitro analysis with B cells (apparent K_D between 5 and 19 nM), was obtained for an average inter-antigen spacing of 2 nm. This distance is required for improving rituximab recognition, and in agreement with the known requirement of CD20 to form clusters to elicit a biological response. More generally, this study offers an interesting outlook in the understanding of the necessity of epitope clusters for effective mAb recognition.

Despite the continuous improvement of traditional chemotherapy, the use of monoclonal antibodies (mAbs) as drugs for the treatment of a variety of diseases has been growing steadily for the last two decades.¹ In this context, there is a strong interest in studying mAb recognition of cognate antigens. MAbs are used in oncology for many therapeutic targets including the CD20 antigen, the human epidermal growth factor receptor 2 (HER2), the vascular endothelial growth factor (VEGF), the epidermal growth factor receptor (EGFR) and the programmed cell death protein 1 (PD-1).² The hematopoietic differentiation antigens associated with cluster of differentiation (CD) represent the main targets for mAb in oncology.³ In particular, the CD20 antigen is the target of several therapeutic mAbs and their derivatives (e.g. rituximab, ibritumomab, ofatumumab, obinutuzumab, ocrelizumab) that are successfully used to treat B-cell malignancies, including non-Hodgkin's lymphoma and chronic lymphocytic leukemia, as well as some autoimmune disorders such as rheumatoid arthritis, systemic lupus erythematosus and multiple sclerosis.⁴

The antigen-binding activity of mAbs determines their biological efficacy and depends on several factors, including antigen density, association and dissociation rates. Several studies have suggested that the increase of CD20 antigen expression modulates the biological response of mAbs such as complement-dependent cytotoxicity (CDC) and antibody-dependent cellular cytotoxicity (ADCC) that trigger cell death.^{5,6,7} As the antigen distribution generally has a direct impact on the clinical efficacies of mAbs, it is of interest to study the influence of CD20 density on mAb recognition. CD20-rituximab (RTX) interactions have been studied in vitro on B-cell lymphoma lines by using flow cytometry or gamma counter experiments.^{8,9} Equilibrium dissociation constants (K_D) in the nanomolar range (5-19 nM) have been reported. These studies, however, did not assess the antigen surface density and distribution. Consequently, it remains unknown how RTX binding to CD20 depends on CD20 surface density, and if the measured dissociation constants are representative of high or low CD20 densities. To date, such information is rarely available for any mAb/antigen combination of clinical relevance highlighting the need for new methods to characterize how mAb recognition depends on antigen density.

Label-free solid-phase interaction assays with highly de-fined biofunctional surfaces can overcome the limitations of cell-based assays, and enable quantitate antigen-antibody interaction analysis. Initial kinetic studies concerning CD20-RTX interactions performed by SPR analysis have shown important variation of the equilibrium dissociation constants (K_D) values, spanning from a few hundred nanomolar to several micromolar.^{10,11} The disparity in K_D values reported for solid-phase versus cell-based binding assays could be related to differences in the accessibility of the immobilized CD20 epitope. In particular, commercial SPR sensors rely on the engrafting of the antigen within a three-dimensional (albeit thin) hydrogel matrix which may impose steric constraints to mAb binding. CD20 as a trans-membrane protein is well-oriented on the cell surface, and one can expect to improve recognition if this two-dimensional antigen presentation was reproduced in SPR assays.

A number of strategies have been reported to immobilize peptide probes onto gold surfaces (as required for SPR) for designing peptide-microarrays¹² or peptide-based biosensors.¹³ These involve the direct adsorption of thiolated peptides (by the way of

cysteine)^{14,15} or a covalent coupling of the peptide to preformed self-assembled monolayers (SAMs) of alkanethiols previously adsorbed on the gold substrate. For the latter purpose, Cu(I)-catalyzed azide-alkyne cycloaddition (CuAAC) has been demonstrated to be well suited for the chemical grafting of peptides onto surfaces via an azide-displaying SAM.¹⁶⁻¹⁹ This chemoselective ligation is generally characterized by quantitative yields and fast reaction kinetics. In addition, the triazole moiety generated by the reaction between azide and alkyne was shown to be remarkably inert resulting in a chemically highly stable peptide-functionalized surface.

In the present work, we have examined the dependence of the binding affinity of RTX on CD20 epitope surface density, which is known to be a critical point for the therapeutic response. To this end, the characterization of the peptide functionalized-surface and the binding assays were achieved by using surface sensitive techniques such as quartz crystal microbalance (QCM-D) and surface plasmon resonance (SPR). These label-free detection techniques provide quantitative information on the amount of CD20 peptide grafted on the SAM gold substrate, and also kinetic and thermodynamic parameters of the binding events between CD20-functionalized surfaces and RTX.

EXPERIMENTAL SECTION

All organic compounds were purchased from VWR International S.A.S. (Fontenay-sous-Bois, France), Sigma-Aldrich (Saint-Quentin Fallavier, France), unless otherwise specified in the text. Rituximab (MabThera) was provided gracefully by Genentech, Inc. (San Francisco, US). Solution of infusion was provided at a concentration of 10 mg/mL (i.e. 69.5 μ M).

Synthesis of CD20 epitope and CD20 scramble. The CD20 peptide used in this study corresponds to a 25-amino-acid sequence that is located in the extracellular part of the full CD20 protein. The CD20 scramble peptide used as a reference was composed of the same amino-acids in a distinct order. The CD20 and CD20 scramble sequences are NIYNCEPANPSEKNSPSTQYCYSIQ and SATNCNSEYQNEPNYIPYSQCKPIS respectively. Whilst both sequences possess a C5-C21 disulfide bridge, all other peptides were in a randomly selected order for the CD20 scramble. Synthesis of the protected peptides was carried out using the Fmoc/*t*-Bu strategy on a peptide synthesizer (Syro2, Biotage) using 2-chlorotriylchloride®. Reaction with 4-pentynoic acid was performed on the resin to incorporate the alkyne function at the N-terminus. After cleavage and removal of protecting groups, formation of disulfide bridges was performed under oxidative conditions. Peptides were then purified by RP-HPLC and their concentration quantified by a UV spectrophotometer (See the supporting information).

QCM-D measurements. Measurements were performed with a Q-Sense E4 system equipped with 4 independent flow modules (Biolin Scientific, Västra Frölunda, Sweden). The system was operated in flow mode with a flow rate of typically 10 μ L/min using a peristaltic pump (ISM935C, Ismatec, Zurich, Switzerland). The working temperature was 25°C. Frequency shifts Δf and dissipation shifts ΔD were measured at six overtones ($n = 3, 5, 7, 9, 11, 13$), corresponding to resonance frequencies of $f_n \approx 5, 15, 25, 35, 45, 55, 65$ MHz; changes in dissipation and normalized frequency, $\Delta f = \Delta f_n/n$, of the seventh overtone ($n = 7$) are presented. Any other overtone would have provided comparable information.

Surface preparation. Prior to each QCM-D measurement, QCM-D sensors were cleaned by rinsing with ultrapure water, blow-drying with N₂ and exposure to UV/ozone (Jelight, Irvine, CA, USA) for 10 min. Within 5 min after UV/ozone treatment, the sensors were immersed in an ethanolic solution of HS-(CH₂)₁₁-(EG)₆-N₃ and HS-(CH₂)₁₁-(EG)₆-OH (ProChimia Surface, Poland), at a total concentration of 1 mM and the desired molar ratio of thiol-azide to thiol-hydroxyle. After overnight incubation, the sensor surfaces were rinsed with ethanol and blow-dried with N₂ gas, before being installed in the QCM-D modules.

Monitoring of the covalent peptide grafting and binding assays using QCM-D. For the covalent peptide grafting, ultrapure water was first injected in the measurement chamber until reaching a stable baseline. DMSO:H₂O (1:1) as running solution was then injected at a standard flow rate of 10 μ L/min. Degassed solutions were injected in the measurement chambers, including CD20 alkyne/CD20-scramble alkyne (200 μ M), CuSO₄ (500 μ M), Tris[(1-benzyl-1H-1,2,3-triazol-4-yl)methyl]amine (TBTA) (500 μ M), and (+)-sodium L-ascorbate (3 mM). After reaching the plateau, the sensor surfaces were rinsed with DMSO:H₂O (1:1). For the binding assay, functionalized surfaces were incubated in PBS (1 \times), citrate (3 mM) and P80 (0.005%) running buffer. Rituximab was then injected in QCM-D module at various concentrations in PBS. The sensor surfaces were rinsed after reaching the plateau. For binding assays carried out for determining the K_D , 30 s injections of Glycine-HCl (10 mM, pH 2) were performed between each RTX concentration.

SPR analysis. SPR data were obtained on a Biacore T200 (GE Healthcare). Measurements were performed on gold surfaces. Sensor chips were cleaned by UV-ozone treatment during 10 min after being rinsed with ultrapure water and ethanol. The cleaned gold surfaces were then functionalized according to the following procedure. Firstly, mixed self-assembled monolayers (SAMs) were formed at room temperature by immersing gold-coated sensors overnight in a thiol mixture of varying percentages of HS-(CH₂)₁₁-EG₆-N₃ and HS-(CH₂)₁₁-EG₄-OH (1 mM total thiol concentration in EtOH). Sensor chips were rinsed with ethanol and blow-dried with nitrogen gas. The surfaces were then inserted in the Biacore T200 device. For the grafting of CD20 antigen, manual runs were conducted with water as running solvent at 2 μ L/min.

The azide-alkyne cycloaddition permitted the covalent grafting of CD20 scramble on channel 1 for the reference, and CD20 on channel 2. Degassed solutions injected are composed of CD20 alkyne/CD20-scramble alkyne (200 μ M), CuSO₄ (500 μ M), Tris[(1-benzyl-1H-1,2,3-triazol-4-yl)methyl]amine (TBTA) (500 μ M), and (+)-sodium L-ascorbate (3 mM), in DMSO:H₂O (1:1). Because the microfluidic system is sensitive to high concentrations of DMSO, the time of injection was controlled and optimized at 8 min for each channel, with a 8 min wait between each injection. The large change of solution refractive index during the injection prevents monitoring of the grafting process in real-time. However, the quantity of immobilized antigen could be evaluated by comparing the shifts in resonance units before and after the injection (Fig. S1 in the supporting information).

The SPR-Biacore experimental conditions were optimized concerning on the one hand the tethering of CD20 (especially the incubation time of CuAAC reactants dissolved in H₂O:DMSO mixture) and on the other hand the composition of the buffer for RTX

binding assays (Fig. S3 in the supporting information). The optimized running buffer (RB) consisted of PBS (1×), citrate (3 mM) and polysorbate P80 (0.005%). Flow cell 1 was functionalized with CD20 scramble to provide a reference surface. Binding assays were conducted using a flow rate of 30 $\mu\text{L}/\text{min}$ at 25°C. The stability of the CD20-functionalized surface was also been checked by achieving tests of repeatability of RTX binding on CD20-functionalized flow-cells (Fig. S5 in the supporting information). RTX dissolved in RB was injected at different concentrations using the high performance method (injection time: 4 min, stabilization time: 10 min). The RTX concentrations investigated are the following: 5, 10, 20, 50, 100, 200, 500, 1000 nM. A regeneration step was necessary between each RTX injection, and was performed by injecting a solution of Glycine-HCl (10 mM, pH 2) for 10 s. Prior to curve fitting analysis, the binding sensorgrams were double-referenced using reference flow cell 1 and preceding buffer blank subtractions to remove the non-specific adsorption of RTX and the change in refractive index respectively. The binding rate constants of CD20/RTX interactions were calculated by a nonlinear analysis of the association and dissociation phases using the SPR kinetic evaluation software of Biacore T200 (evaluation Software 2.0.1). The data were fitted using a heterogeneous ligand model, which provides the best fitting (Fig. S6 in the supporting information). The reported values are the average of representative independent experiments and the errors provided are standard deviations from the mean. Each SPR experiment was repeated at least four times.

Fab generation. RTX Fab fragments were generated from papain digestion of the mAb by using the Pierce Fab preparation kit (Thermo Scientific) and following the given instructions. Fab fragments were then purified with column provided by the kit. The digestion was checked by SDS-PAGE (Fig. S8 in the supporting information), and Fab fragments concentration was measured by UV.

RESULTS AND DISCUSSION

Control and characterization of CD20 density on gold substrates. We used the extracellular loop of the CD20 protein (amino acids N163 to Q187) which is known to be the binding epitope of RTX.²⁰ This peptide was prepared by classical solid-phase peptide synthesis and a disulfide bridge formation in buffered solution (see the supporting information). We introduced an alkyne function at the N-terminus for CuAAC coupling to preformed SAM surfaces displaying azide groups (Fig. 1), as previously described.^{21,22} Thanks to this site-specific ligation, and the disulfide bridge present in the natural peptide sequence, the CD20 epitope is displayed with a defined orientation and conformation that recapitulates the presentation of the extracellular CD20 loop on the cell surface.²⁰ The SAM contained alkanethiolates with terminal-oligo(ethyleneglycol) (OEG) that provides physical rigidity in combination with chemical flexibility. Moreover, the OEG-alkanethiols form a bioinert background conferring resistance to non-specific protein adsorption.²³ The SAMs presenting azide were adsorbed on gold substrates by incubating thiol solutions with varying molar ratios of HS-(CH₂)₁₁-(EG)₆-N₃ (thiol-azide) and HS-(CH₂)₁₁-(EG)₄-OH (thiol-hydroxyle). By using thiol-azide fractions ranging from 0.1% to 50%, we were able to design functional surfaces with tunable coverages of the CD20 epitope (Fig. 1, Fig S2 in the supporting information).

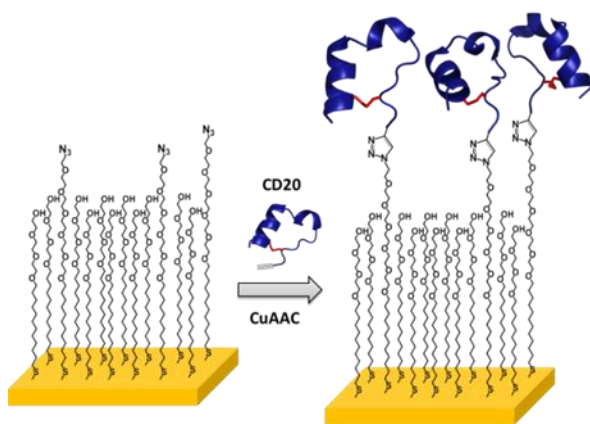


Figure 1. Schematic representation of the CD20 epitopes grafting onto a preformed SAM-azide by CuAAC. The disulfide bridge is shown in red.

In order to control the CD20 surface coverage, two mass-sensitive surface techniques, QCM-D and SPR, were employed. While no measurable change in QCM-D signals (i.e. shifts in frequency, f , and dissipation, D) was recorded during the injection of CD20 solution without the CuAAC reactants in the flow chamber, a fast decrease in frequency was observed when the reaction mixture containing the CD20 epitope was injected, indicating covalent grafting of CD20 to the SAM-gold substrate (Fig. S9-S10 in the supporting information). Rinsing with pure solvent led to stable signals showing the stability of CD20-functionalized surfaces, and thus providing further evidence of the chemical grafting of the peptide to the surface. The QCM-D traces showed only small shifts in dissipation after CD20-functionalization, indicating that the CD20 epitope form a relatively rigid film. The Sauerbrey relation (Eq. S2) can thus be applied for the determination of the acoustic mass (m_{QCM} ; Table 1). QCM-D provides hydrated masses (mass of CD20 layer with hydrodynamically coupled water) which show increasing values until reaching a maximum at 432 ng/cm^2 for 12.5% of thiol-azide.

Following the procedure as established by QCM-D, the covalent grafting of CD20 was transferred to SPR sensors. Grafting was carried out inside the Biacore apparatus onto SAM-functionalized sensor chips, as this enabled different measurement channels to be functionalized with various peptides. In particular, a scramble containing the same amino acids as the CD20 peptide but in a different random order was chosen as reference to be able to correct for variations in the solution refractive index and/or spurious non-specific interactions.

To the best of our knowledge, there are very few examples of *in situ* grafting of SPR sensor chips through CuAAC using an SPR apparatus equipped with a microfluidic system.²⁴ To prevent damage to the microfluidic system, the hydro-organic solution (H₂O/DMSO) containing the click chemistry reactants was injected only for a short time (8 min) in the flow cells (Fig. S1 in the supporting information). An additional benefit of the *in situ* click chemistry is that it allows quantitating the amount of grafted CD20 from the change in the SPR signal. By using Jung's formula (Eq. S1 in the supporting information) the magnitude of the response units (RU) was converted into areal mass densities. Jung's formula requires the SAM and CD20 to be considered as separate layers, and the layer thicknesses to be known. These were measured by spectroscopic ellipsometry (SE) (See the supporting information). Whatever the azide percentage, the thickness of the SAM was found to be of 2.5 ± 0.5 nm, in accordance with previous results (2.6 nm).²⁵ After CD20 grafting at saturation, an additional film thickness of 4.6 ± 0.2 nm was found. The areal mass densities of CD20 calculated from SPR experiments show that the immobilization capacity of the SAM-azide substrate increases monotonously with the number of azide reactive functions across the probed range from 0 to 50% of thiol-azide (Table 1). A comparison of the areal mass densities measured by QCM-D (m_{QCM} ; hydrated mass) and by SPR (m_{SPR} ; dry mass) provides a measure of the CD20 film hydration (Eq. S3 in the supporting information): the hydration is high (92%) for low CD20 density (2.8 pmol.cm^{-2} corresponding to m_{SPR} of 8 ng.cm^{-2}) and decreases for denser CD20 layers, down to 38% at 85 pmol.cm^{-2} ($m_{\text{SPR}} = 249 \text{ ng.cm}^{-2}$). The decrease of coupled water induced by lowering the surface coverage as sensed by QCM-D has ever been reported and modeled for globular proteins.²⁶ The authors showed that the hydration curves could be well fitted by a straight line by using a model that ascribed a hydration coat (truncated pyramid-shaped) to each adsorbed biomolecule. Furthermore, we noticed that to reach a CD20 surface density of 46 pmol.cm^{-2} ($m_{\text{SPR}} = 135 \text{ ng.cm}^{-2}$) only 6% of azide-presenting alkanethiols would be required in the SAM (since total alkanethiol surface density is $7.3 \cdot 10^{-10} \text{ mol.cm}^{-2}$).²² The mismatch with the 12.5% thiol-azide used in the solution to prepare the SAMs is likely due in part to preferential binding of the thiol-hydroxyl, as previously reported.²² Additionally, for high thiol-azide densities, the CuAAC reaction may be incomplete due to steric hindrance of CD20 on surface.

Assuming a random distribution of CD20 epitopes on the SAM surface, root-mean-square (rms) distances between adjacent CD20 epitopes were calculated based on the SPR data. Values ranging from 9.1 to 1.4 nm were obtained for surfaces prepared with thiol-azide fractions ranging from 0.1% to 50%, respectively (Table 2).

Table 1. Influence of thiol-azide molar ratio on CD20 areal mass densities.

N ₃ (%)	$-\Delta f_7$ (Hz)	m_{QCM}^a (ng.cm ⁻²)	SPR resp. ^b (RU)	m_{SPR}^c (ng.cm ⁻²)	Hydration (%)
0.1	nd	nd	60 ± 11	6 ± 1	nd
1	5.6 ± 0.2	100 ± 4	82 ± 22	8 ± 2	92 ± 2
2.5	14 ± 2.0	251 ± 3	694 ± 118	69 ± 12	72 ± 1
12.5	24 ± 1.0	432 ± 9	1352 ± 308	135 ± 31	69 ± 7
20	23.4 ± 1.3	421 ± 23	1642 ± 381	164 ± 38	61 ± 7
50	22.4 ± 0.6	404 ± 11	2488 ± 145	249 ± 14	38 ± 2

nd = not determined. (a) Acoustic mass determined with Sauerbrey equation and 7th overtone. (b) SPR Response corresponding to the change of baseline magnitude before and after grafting. (c) Optical mass calculated following Jung's formula (Eq. S1 in the supporting information).

Effect of CD20 density on rituximab recognition. The specificity of the resulting CD20 functionalized surface towards RTX binding affinity was again evaluated by QCM-D and SPR. Using QCM-D, a comparison of two functionalized-surfaces displaying the CD20 epitope and the CD20 scramble respectively clearly demonstrated successful and fully selective binding of RTX (10 nM) to CD20 (Fig. S9 in the supporting information). Additional SPR experiments were carried out to confirm the specificity of the recognition event. Injection of RTX (at 1 μM) to a surface presenting the CD20 epitope led to a response of 1800 RU, whereas only 100 RU were measured with the CD20 scramble and 60 RU with a pure and inert alkanethiolate SAM (Fig. 2). We attribute the 60 RU shift to refractive index effects (which are known to sensitively affect the SPR response), and the difference of 40 RU to non-specific binding. Thus, non-specific binding was very low, justifying the use of the CD20 scramble as the reference channel in all subsequent analyses. Moreover, the complete absence of a response (after subtraction of the reference channel) for an equal concentration of trastuzumab, a mAb which belongs to the same IgG subclass, demonstrates the specificity of the CD20 surface for RTX (Fig. 2, orange curve, Fig. S4, Fig. S12 in the supporting information).

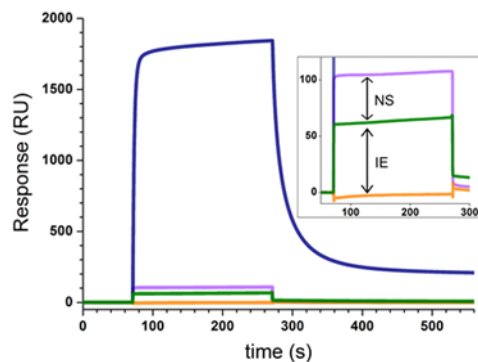


Figure 2. SPR sensorgrams representing control experiments. Raw curves are shown for RTX injections at 1 μM onto SAMs with CD20 epitope (blue), with a CD20 scramble (purple), and without any peptide functionalization (pure thiol-hydroxyle; green). Inset: Zoom into a part of the data. The response on the peptide-free surface is caused by refractive index differences between the pure and mAb containing solutions, whereas the small additional response on the CD20 scramble likely reflects minor and transient non-specific (NS) mAb binding. The specificity of CD20 antigen for RTX is evaluated by the injection of trastuzumab (1 μM) onto the CD20 flow cell (orange curve obtained after subtraction of CD20 scramble reference data). The CD20 and CD20 scramble surfaces were made from functionalized SAM (prepared with 20% thiol azide) bearing 56 $\text{pmol}\cdot\text{cm}^{-2}$ peptide.

SPR binding assays were then carried out to determine the kinetic parameters of the RTX-CD20 interaction as a function of CD20 surface density. Figure 3 depicts the recorded binding response profiles for three different CD20 surface densities. The sensorgram shapes along with the magnitude of the equilibrium responses show a dependence of RTX binding on the ligand density in the following rank order: $46 > 2.8 > 85 \text{ pmol}\cdot\text{cm}^{-2}$. Figure 3B shows a saturation for the SPR signal at 500 nM (2000 RU) while for 2.8 $\text{pmol}\cdot\text{cm}^{-2}$ (Fig. 3A) and 85 $\text{pmol}\cdot\text{cm}^{-2}$ (Fig. 3C) the SPR responses did not reach the saturation (1000 RU and 450 RU for 1 μM , respectively). It is important to note that for the highest CD20 surface density the affinity is the lowest. An enhancement of the affinity with the increase of the CD20 surface density until reaching a plateau was expected.

The so-called heterogeneous ligand (HL) model was used to extract kinetic parameters, i.e. the on-rate (k_{on}) and off-rate (k_{off}), from the data (Fig. S6-S7, table S1, in the supporting information). This model allows interactions with up to two ligand species with distinct kinetic parameters. The deconvolution of the modeled curves revealed that one interaction was generally dominant. The second interaction exhibited low magnitude, and the shape of the curves (for the second interaction) was characteristic of a non-specific interaction. We hypothesize that the second interaction is related to soluble RTX aggregates which can interact with CD20 surface, as self-association of RTX has been already mentioned in the literature.²⁷ The fitted data based on the HL model are presented on the sensorgrams in figure 3 for the association and dissociation phases corresponding to the mAb interaction. The apparent K_D determined either by using the kinetic data ($k_{\text{off}}/k_{\text{on}}$ ratio) or by a Langmuir binding isotherm plotted from the sensorgrams at steady-state equilibrium are similar (Table 2).

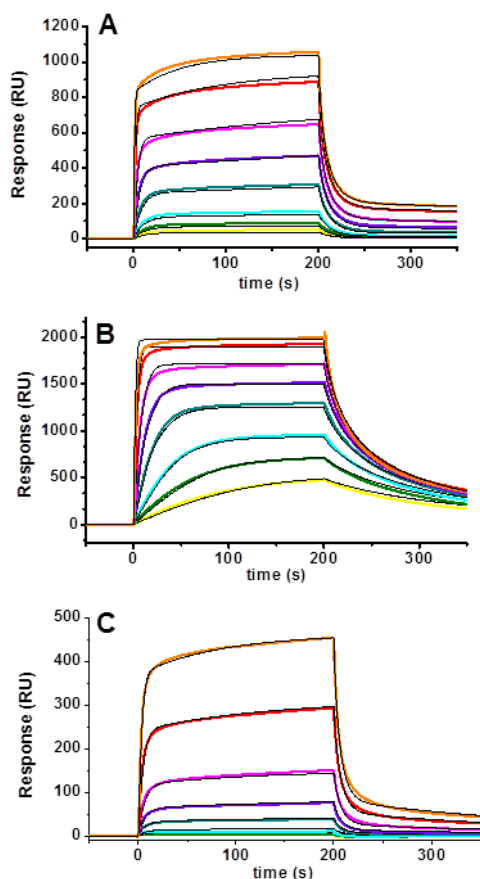


Figure 3. RTX-CD20 SPR binding profiles. Sensorgrams were recorded at different CD20 surface densities: (A) 2.8 pmol.cm⁻², (B) 46 pmol.cm⁻², and (C) 85 pmol.cm⁻². RTX concentrations were ranging from 5 to 1000 nM (5, 10, 20, 50, 100, 200, 500 and 1000 from yellow to orange curves). The sensorgrams were fitted with the heterogeneous ligand kinetic model (RI correction = 0) and the fitted curves were added to the graph (black curves).

Figure 4A depicts the evolution of these apparent K_D values as a function of CD20 surface density. It clearly shows a dependence of the ligand density on the RTX binding affinity. At low antigen density (2.1 pmol.cm⁻²), the K_D value is extremely high (977 ± 8 nM). When increasing the CD20 densities, the K_D values decrease until reaching a minimum of 32 nM for a surface displaying around 46 pmol.cm⁻² of CD20 epitope, which appears to be the optimal surface density. Interestingly, the apparent maximum response obtained at 46 pmol.cm⁻² CD20 ($K_D = 32$ nM) is close to the values reported from *in vitro* analysis performed by flow cytometry with CD20-expressing cells (5-19 nM).^{8,9} Increasing the CD20 epitope density beyond 46 pmol.cm⁻² to 85 pmol.cm⁻², was accompanied by a dramatic increase of K_D to values in the micromolar range. Such evolution can be rationalized by the influence of the average inter-antigen distance on the RTX binding affinity on the antigenic surface. Compactness of the CD20 layer is expected when the inter-antigen distance decreases. Correlating with the K_D evolution, we observe an inverse variation of the maximum SPR responses (R_{max} values) as shown the figure 4B. The maximum binding capacity of RTX is observed for 46 pmol.cm⁻² (corresponding to the minimal K_D), whereas R_{max} values fall down afterwards, meaning that less mAbs interact with the surface at high surface density. This result can be assigned to the high compactness of the layer due to CD20-CD20 interaction that makes the CD20 epitope less available for RTX binding.

By using a previously reported model,^{28,29} we were able to estimate the fraction of surface-grafted antigens that is available for RTX binding. Based on consideration of antibody size and antigen surface density, CD20 epitopes already engaged in RTX interaction or effectively obstructed by a surrounding RTX were excluded to estimate the fraction of antigens accessible for additional binding (Fig. S13, Eqs. S4-5, in the supporting information). For a CD20 density of 46 pmol.cm⁻², only 20% of CD20 are available for a subsequent RTX rebinding (Fig. S13 in the supporting information). Under this circumstance, the R_{max} cannot be enhanced further above a grafting density of 50-60 pmol.cm⁻². Furthermore, high densities of CD20 could generate CD20-CD20 interaction that inhibits the binding of mAb.

In addition to SPR analysis, an apparent binding affinity was determined by QCM-D (Table S2, Eq. S6, Fig. S14 in the supporting information) from the shift in frequency measured for various RTX concentrations on surfaces displaying 2.8, 46 and 85 pmol.cm⁻² of CD20 epitope. As expected, similar results were observed and a minimal K_D was obtained for 46 pmol.cm⁻² (Table S2 in the supporting information).

Furthermore, K_D -related observations can be made for kinetic parameters, especially for k_{on} values that tend to follow similar variation. Table 2 shows a 10-fold increase in k_{on} for CD20 densities between 2.1 pmol.cm⁻² (4.7×10^5 M⁻¹.s⁻¹) and 23.7 pmol.cm⁻² (45.6×10^5 M⁻¹.s⁻¹). This density range corresponds to the growth of available CD20-containing surface densities until reaching a plateau corresponding to 46 pmol.cm⁻² (Fig. S7 in the supporting information). Values of k_{on} increase with the amount of antigens on the surface, while K_D values decrease. In contrast, for high CD20 densities ($\Gamma_{CD20} > 46$ pmol.cm⁻²), the drop in k_{on} is explained by CD20-CD20 interaction on surface that reduces their accessibility. Such results have already been reported in the literature.³⁰

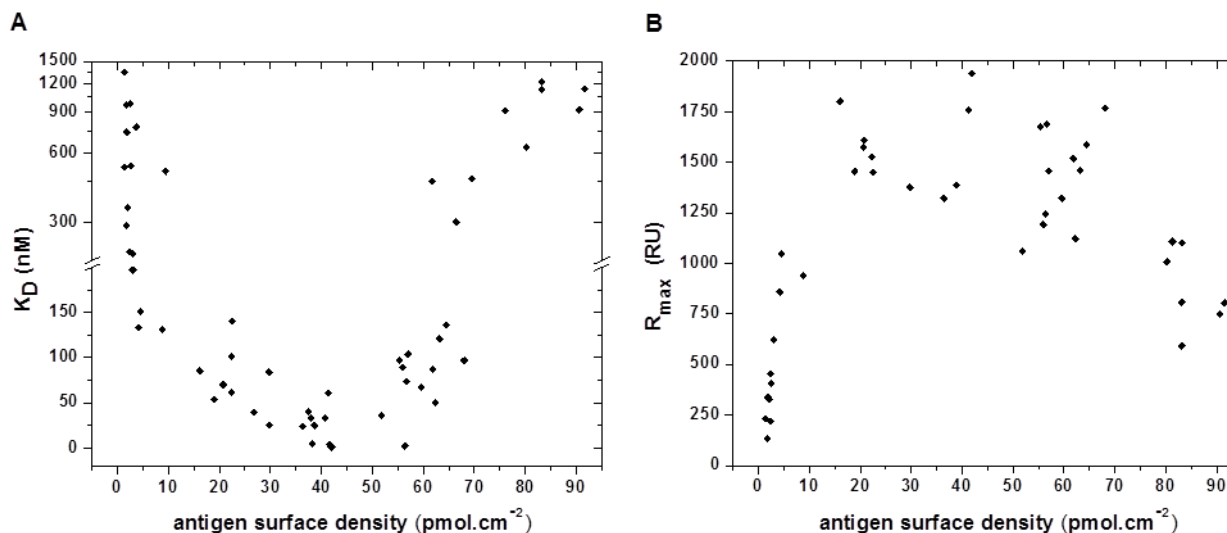


Figure 4. Impact of CD20 density on RTX binding affinity. (A) Binding affinity, (B) R_{max} measured for RTX (K_D and R_{max} were determined by kinetic data). The antigen surface density was calculated with Jung's formula, starting from the resonance response unit (RU) corresponding to the *in situ* covalent grafting of CD20 epitope to the sensor chips.

Table 2. Inter-antigen spacing, kinetic and thermodynamic parameters for CD20 / RTX binding as a function of CD20 surface density.

N ₃ (%)	Γ_{CD20} (pmol.cm ⁻²) ^a	Inter-antigen spacing (nm) ^b	k_{on} (RTX) (10 ⁵ M ⁻¹ .s ⁻¹)	k_{off} (RTX) (s ⁻¹)	K_D (Kinetic) (nM)	K_D (Steady- state) (nM)
0.1	2.1 ± 0.4	9.1 ± 0.8	4.7 ± 1.3	0.46 ± 0.02	977 ± 8	694 ± 37
1	2.8 ± 0.8	7.4 ± 1.2	17.7 ± 7.1	0.46 ± 0.24	248 ± 94	273 ± 72
2.5	23.7 ± 4.0	2.7 ± 0.2	45.6 ± 6.8	0.35 ± 0.07	75 ± 6	98 ± 9
12.5	46.1 ± 10.5	2.0 ± 0.2	27.5 ± 9.3	0.08 ± 0.03	32 ± 12	25 ± 12
20	56.0 ± 13.0	1.8 ± 0.2	17.3 ± 2.2	0.27 ± 0.06	152 ± 16	181 ± 16
50	84.9 ± 4.9	1.4 ± 0.0	4.4 ± 2.6	0.47 ± 0.32	1007 ± 16	1156 ± 114

(a) CD20 Surface density on SPR sensor chip determined by Jung's formula. (b) Root-mean-square distances between two CD20 epitopes calculated from the surface densities.

Concurrently, values of k_{off} decrease significantly with increasing densities until a minimal value ($k_{off} = 0.08$ s⁻¹) at 46 pmol.cm⁻². For high CD20 densities, values of k_{off} increase to about 0.4 s⁻¹ (Table 2).

All these variations are consistent with a high probability of a statistical rebinding of the mAb together with the occurrence of potential bivalent binding when CD20 density reaches an optimal value with sufficient inter-antigen distance while maintaining good accessibility of the antigen (Fig. 5). These two phenomena cannot be discriminated using SPR. This technique measures the change in the refractive index near the surface. The change in refractive index is proportional to the total amount of RTX in close proximity to the surface but cannot discriminate those which are bound by one arm to those bound by two arms.

The effect of antigen surface density on the binding affinity of antibodies has been already reported in the literature, for instance for HIV-1 neutralizing antibodies interacting with gp120 glycoprotein.³¹ The data reveal that the extent of the changes of the binding energetics as a function of antigen density strongly depend on the binding affinity of each antibody. The authors observed a marked increase in avidity to variation in antigen density in the case of low to moderate binding affinity whereas the impact of antigen immobilization is very low for antibodies exhibiting high affinity.

To better understand the gain of affinity due to the statistical rebinding and to the bivalency of the mAb, RTX Fab fragments were used for SPR binding assays (Fig. S15, in the supporting information). Table 3 shows the kinetic parameters obtained for the Fab on surfaces displaying 2.8 and 46 pmol.cm⁻² of CD20. We observe that k_{on} and k_{off} values are affected when increasing the CD20 surface density. These concomitant variations are supported by the change in accessibility of CD20 epitope which is dependent on the CD20 surface density resulting in a significant increase of K_D (12700 vs 617 nM, for 2.8 and 46 pmol.cm⁻² of CD20 respectively). Interestingly, the k_{off} value for the Fab ($0.64 \times 10^5 \text{ M}^{-1} \cdot \text{s}^{-1}$) is similar to the one obtained for RTX ($0.46 \times 10^5 \text{ M}^{-1} \cdot \text{s}^{-1}$) for surface displaying 2.8 pmol.cm⁻² of CD20. This result suggests that statistical rebinding is restricted on surface displaying low CD20 density (Figure 5). On the contrary, the rate of association for the Fab is around 30-fold lower than for the bivalent mAb ($0.6 \text{ vs } 17.7 \times 10^5 \text{ M}^{-1} \cdot \text{s}^{-1}$) (See Fig S16, in the supporting information). Such discrepancies can be explained by the bivalency of the RTX/CD20 interaction and the flexibility of the two Fab arms (3-14 nm) that would allow the mAb a wider search range for CD20 binding sites compared to Fab. The enhancement of avidity afforded by the bivalency of RTX is more pronounced for a CD20 surface density of 2.8 pmol.cm⁻². Consequently, k_{on} is greatly affected by these phenomena. Such comparison underlines the bivalency effect for the association of RTX when antigen density is low. For surface density of 46 pmol.cm⁻² of CD20, the k_{off} values for the Fab (0.2 s^{-1}) and for the RTX (0.08 s^{-1}) point out the high probability of RTX rebinding on CD20 surface. Intrinsic flexibility of the mAb allows exploring large surface as the distance between both active sites (paratope) varies from 3 to 14 nm.³² Together these results show how important is the role of the second arm on the RTX binding capacities, as it improves the affinity of the mAb for the surface and its statistical rebinding (Figure 5). Regarding the K_D values, a strong difference is observed for 2.8 pmol.cm⁻² ($K_D = 12700 \text{ nM}$ for Fab vs $K_D = 248 \text{ nM}$ for RTX) and, to a lesser extent, for 46 pmol.cm⁻² ($K_D = 617 \text{ nM}$ for Fab vs $K_D = 32 \text{ nM}$ for RTX), leading to Fab/RTX K_D ratios of 51 and 19 respectively. These data are in accordance with values from the literature. Whitesides et al. reported a 50-fold enhancement of binding for a synthetic bivalent protein dimer (mimicking mAb) compared to the monovalent one interacting with mixed SAMs presenting ligands.³³ It is worth noting that the contribution of the surface densities can be isolated by comparing the K_D values related to RTX Fab - CD20 interaction at 2 and 46 pmol.cm⁻². It turns out that a 21-fold factor is observed from low to medium antigen grafting density. As RTX Fab is a monovalent molecule, improvement of affinity is exclusively due to surface densities, improving the rate of association, and the rate of dissociation via rebinding process. We have to underline that this phenomenon also exists for the mAb-CD20 recognition but to a lesser extent, 7-fold factor ($K_D = 248 \text{ nM}$ for density of 2.8 pmol.cm⁻² vs 32 nM for 46.1 pmol.cm⁻²). This result confirms that the contribution of bivalency is critical for both the mAb association, but also for the statistical rebinding. The rebinding process was described by Preiner et al. as a stochastic walking of IgGs on 2D rigid surfaces.³⁴ The authors demonstrated by high speed atomic force microscopy that the moving speeds and step sizes are dependent of the antigen density.

Table 3. Kinetic parameters for the CD20 / RTX Fab binding.

N ₃ (%)	Γ_{CD20} (pmol.cm ⁻²) ^a	k_{on} (RTX Fab) (10 ⁵ M ⁻¹ .s ⁻¹)	k_{off} (RTX Fab) (s ⁻¹)	K_D (Kinetic) (nM)
1	2.8 ± 0.8	0.6 ± 0.2	0.64 ± 0.12	12700 ± 3750
12.5	46.1 ± 10.5	3.8 ± 0.8	0.2 ± 0.02	617 ± 74

(a) CD20 Surface density on SPR sensor chip determined by Jung's formula.

To date, there is evidence supporting the impact of CD20 distribution on the clinical efficacies of RTX.^{6,7,35} Antigen density is a critical parameter that determines the biological efficacy of the mAb especially *via* the complement-induced cell death. Additionally, microscopy experiments of fluorescent RTX showed a heterogeneous distribution of CD20 antigens on the cell surface,⁸ suggesting that CD20 proteins are organized into clusters.³⁶ In our study, the highest affinity was determined for a CD20 surface density of 46 pmol.cm⁻² which corresponds to an average inter-antigen spacing of around 2 nm (Table 2). Considering the size of CD20-expressing B cells (around 8 μm in diameter) and the amount of CD20 antigens per cells ($2 \text{ to } 6 \times 10^5$),^{5,8,37} a homogeneous distribution would imply areal mass densities of 0.003 to 0.6 pmol.cm⁻². According to our SPR experiments, these values (average inter-antigen spacing above 7 nm) correspond to surfaces that did not allow strong RTX binding (Fig. 5, Table 2). Together, our results provide strong evidence for a nanoscale distribution of CD20 and the requirement of an average critical inter-antigen spacing of 2 nm for RTX binding. We suggest that this critical CD20 density is required within CD20 clusters on cell surface for efficient RTX binding.

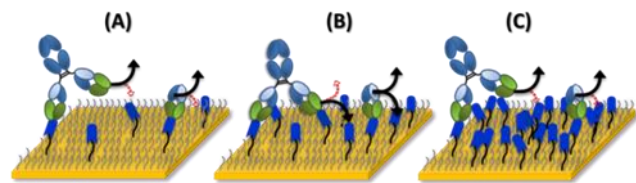


Figure 5. Schematic of rebinding phenomena occurring on surfaces displaying CD20 surface densities during the rinsing step: (A) low, (B) medium, (C) high CD20 surface densities. At low and high antigen surface density, the antibody is mostly bound through one arm like the Fab, and is quickly removed from the surface (A and C). At medium antigen surface density (46 pmol.cm⁻²), the probability of the mAb to bind with the two arms and to find a neighboring antigen after dissociation of one of its arm is high, leading to a lower k_{off} , and so a stronger avidity.

CONCLUSION

In this study, we designed surfaces with tunable areal mass densities of the CD20 epitope. We were able to study the contribution of the statistical rebinding and the bivalent effect of RTX mAb, especially through a comparison with the RTX Fab. An average critical inter-CD20 spacing of nearly 2 nm was found that confers the best conditions for RTX binding. This nanoscale distribution corroborates the prerequisite CD20 cluster formation for biological activity of RTX. It is expected that this inter-antigen spacing might be required for other mAbs as well. Additionally, we reason that the design of such surfaces will pave the way for the discovery of mAb mimics, especially through the screening of peptides, nucleic acid aptamers or phage libraries.

ASSOCIATED CONTENT

Supporting Information

Detailed description on the CD20 epitope synthesis (HPLC and mass analysis) and additional SPR sensorgrams and QCM-D profiles were available in the supporting information. The Supporting Information is available free of charge on the ACS Publications website.

AUTHOR INFORMATION

Corresponding Author

* E-mail: didier.boturny@univ-grenoble-alpes.fr.

Present Addresses

†If an author's address is different than the one given in the affiliation line, this information may be included here.

Author Contributions

The manuscript was written through contributions of all authors. All authors have given approval to the final version of the manuscript.

ACKNOWLEDGMENT

This work was supported by the CNRS, the University Grenoble Alpes, the “Communauté d’agglomération Grenoble-Alpes Mét-ropole” (Nanobio program) and by the “Agence Nationale de la Recherche” including “Mimobody” research support (ANR-13-BS07-0014-01) and LabEx ARCANE and CBH-EUR-GS (ANR-17-EURE-0003). Laure Bar acknowledges the “Groupe français des peptides et des protéines” (GFPP) for a grant to cover travel to Leeds for SE experiments. The authors wish to acknowledge the support from the ICMG chemistry platform, Grenoble, on which the peptide synthesis has been performed, the ICMG PCI platform, Grenoble, on which analyses were done, and Genentech, Inc. (San Francisco), a member of Roche group, for providing Rituximab.

REFERENCES

- (1) Ecker, D. M.; Dana Jones, S.; Levine, H. L. The therapeutic monoclonal antibody market. *mAbs* **2015**, *7*, 9-14.
- (2) Twomey, J. D.; Brahme, N. N.; Zhang, B. Drug-biomarker co-development in oncology - 20 years and counting. *Drug Resist. Update* **2017**, *30*, 48-62.
- (3) Scott, A. M.; Wolchok, J. D.; Old, L. J. Antibody therapy of cancer. *Nature* **2012**, *12*, 278-287.
- (4) Klein, C.; Lammens, A.; Schäfer, W.; Georges, G.; Schwaiger, M.; Mössner, E.; Hopfner, K.-P.; Umaña P.; Niederfellner, G. Epitope interactions of monoclonal antibodies targeting CD20 and their relationship to functional properties. *mAbs* **2013**, *5*, 22-33.
- (5) Singh, V.; Gupta, D.; Arora, R.; Tripathi, R. P.; Almasan, A.; Macklis, R. M. Surface levels of CD20 determine Aanti-CD20 antibodies mediated cell death *in vitro*. *PLoS One* **2014**, *9*, e111113. doi: 10.1371/journal.pone.0111113.
- (6) Van Meerten, T.; Van Rijn, R. S.; Hol, S.; Hagenbeek, A.; Ebeling, S. B. Complement-induced cell death by rituximab depends on CD20 expression level and acts complementary to antibody-dependent cellular cytotoxicity. *Clin. Cancer Res.* **2006**, *12*, 4027-4035.
- (7) Li, M.; Xiao, X.; Zhang, W.; Liu, L.; Xi, N.; Wang, Y. Nanoscale distribution of CD20 on B-cell lymphoma tumour cells and its potential role in the clinical efficacy of rituximab. *J. Microsc.* **2014**, *254*, 19-30.
- (8) Melhus, K. B.; Larsen, R. H.; Stokke, T.; Kaalhus, O.; Selbo, P. K.; Dahle, J. Evaluation of the binding of radiolabeled rituximab to CD20-positive lymphoma cells: an *in vitro* feasibility study concerning low-dose-rate radioimmunotherapy with the α -emitter ^{227}Th . *Cancer Biother. Radiopharm* **2007**, *22*, 469-479.
- (9) Reff, M. E.; Carner, K.; Chambers, K. S.; Chinn, P. C.; Leonard, J. E.; Raab, R.; Newman, R. A.; Hanna, N.; Anderson, D. R. Depletion of B cells *in vivo* by a chimeric mouse human monoclonal antibody to CD20. *Blood* **1994**, *83*, 435-445.
- (10) Blasco, H.; Lalmanach, G.; Godat, E.; Maurel, M.C.; Canepa, S.; Belghazi, M.; Paintaud, G.; Degenne, D.; Chatelut, E.; Cartron, G.; Le Guellec, C. Evaluation of a peptide ELISA for the detection of rituximab in serum. *J. Immunol. Methods* **2007**, *325*, 127-139.
- (11) Liu, J. L.; Zabetakis, D.; Goldman, E. R.; Anderson, G. P. Selection and characterization of single domain antibodies against human CD20. *Mol. Immunol.* **2016**, *78*, 146-154.
- (12) Gori, A.; Longhi, R. *Peptide Microarrays: Methods and Protocols* (eds. Cretich, M. & Chiari, M.) **2016**, 145-156.
- (13) Puiu, M.; Bala, C. Peptide-based biosensors: From self-assembled interfaces to molecular probes in electrochemical assays. *Bioelectrochemistry* **2018**, *120*, 66-75.
- (14) Puiu, M.; Bala, C. Building switchable peptide-architectures on gold/composite surfaces: New perspectives in electrochemical bioassays. *Curr. Opin. in Electrochemistry* **2018**, *12*, 13-20.
- (15) Leo, N.; Liu, J.; Archbold, I.; Tang, Y.; Zeng, X. Ionic strength, surface charge, and packing density effects on the properties of peptide self-assembled monolayers. *Langmuir* **2017**, *33*, 2050-2058.
- (16) Hudalla, G. A.; Murphy, W. L. Using “Click” chemistry to prepare SAM substrates to study stem cell adhesion. *Langmuir* **2009**, *25*, 5737-5746.
- (17) Gerasimov, J. Y.; Lai, R. Y. Design and characterization of an electrochemical peptide-based sensor fabricated via “click” chemistry. *Chem. Commun.* **2011**, *47*, 8688-8690.

- (18) Gori, A.; Cretich, M.; Vanna, R.; Sola, L.; Gagni, P.; Bruni, G.; Liprino, M.; Gramatica, F.; Burastero, S.; Chiari, M. Multiple epitope presentation and surface density control enabled by chemoselective immobilization lead to enhanced performance in IgE-binding fingerprinting on peptide microarrays. *Anal. Chim. Acta* **2017**, *983*, 189-197.
- (19) Raigoza, A. F.; Onyirihoa, K.; Webb, L. J. Controlling noncovalent interactions between a lysine-rich α -helical peptide and self-assembled monolayers of alkanethiols on Au through functional group diversity. *Appl. Surf. Sc.* **2017**, *396*, 1831-1839.
- (20) Du, J.; Wang, H.; Zhong, C.; Peng, B.; Zhang, M.; Li, B.; Huo, S.; Guo, Y.; Ding, J. Structural basis for recognition of CD20 by therapeutic antibody rituximab. *J. Biol. Chem.* **2007**, *282*, 15073-15080.
- (21) Degardin, M.; Thakar, D.; Claron, M.; Richter, R. P.; Coche-Guérente, L.; Boturyn, D. Development of a selective cell capture and release assay: impact of clustered RGD ligands. *J. Mater. Chem. B* **2017**, *5*, 4745-4753.
- (22) Dubacheva, G. V.; Van Der Heyden, A.; Dumy, P.; Kaftan, O.; Auzély-Velty, R.; Coche-Guerente, L.; Labbé, P. Electrochemically controlled adsorption of Fc-functionalized polymers on β -CD-modified self-assembled monolayers. *Langmuir* **2010**, *26*, 13976-13986.
- (23) Prime, K. L.; Whitesides, G. M. Adsorption of proteins onto surfaces containing end-attached oligo(ethylene oxide): a model system using self-assembled monolayers. *J. Am. Chem. Soc.* **1993**, *115*, 10714-10721.
- (24) Ta, D. T.; Guedens, W.; Vranken, T.; Vanschoenbeek, K.; Redeker, E. S.; Michiels, L.; Adriaensens, P. Enhanced biosensor platforms for detecting the atherosclerotic biomarker VCAM1 Bbased on bioconjugation with uniformly oriented VCAM1-targeting nanobodies. *Biosensors* **2016**, *6*, 34. doi: 10.3390/bios6030034.
- (25) Solano, I.; Parisse, P.; Gramazio, F.; Cavalleri, O.; Bracco, G.; Castronovo, M.; Casalis, L.; Canepa, M. Spectroscopic ellipsometry meets AFM nanolithography: about hydration of bio-inert oligo(ethylene glycol)-terminated self assembled monolayers on gold. *Phys. Chem. Chem. Phys.* **2015**, *17*, 28774-28781.
- (26) Bingen, P.; Wang, G.; Steinmetz, N. F.; Rodahl, M.; Richter, R. P. Solvation effects in the quartz crystal microbalance with dissipation monitoring response to biomolecular adsorption. A phenomenological approach. *Anal. Chem.* **2008**, *80*, 8880-8890.
- (27) Morgan, H.; Tseng, S.-Y.; Gallais, Y.; Leineweber, M.; Buchmann, V.; Riccardi, S.; Nabhan, M.; Lo, J.; Gani, Z.; Szely, N.; Zhu, C. S.; Yang, M.; Kiessling, A.; Vohr, H.-W.; Pallardy, M.; Aswad, F.; Turbica, I. Evaluation of *in vitro* assays to assess the modulation of dendritic cells functions by therapeutic antibodies and aggregates. *Front. Immunol.* **2019**, *10*: 601. doi: 10.3389/fimmu.2019.00601.
- (28) Yang, T.; Baryshnikova, O. K.; Mao, H.; Holden, M. A.; Cremer, P. S. Investigations of bivalent antibody binding on fluid-supported phospholipid membranes: the effect of hapten density. *J. Am. Chem. Soc.* **2003**, *125*, 4779-4784.
- (29) Hlavacek, W. S.; Posner, R. G.; Perelson, A. S. Steric effects on multivalent ligand-receptor binding: exclusion of ligand sites by bound cell surface receptors. *Biophys. J.* **1999**, *76*, 3031-3043.
- (30) Jung, H.; Robison, A. D.; Cremer, P. S. Multivalent ligand-receptor binding on supported lipid bilayers. *J. Struct. Biol.* **2009**, *168*, 90-94.
- (31) Hadzhieva, M.; Pashov, A. D.; Kaveri, S.; Lacroix-Desmazes, S.; Mouquet, H.; Dimitrov, J. D. Impact of antigen density on the binding mechanism of IgG antibodies. *Sci. Rep.* **2017**, *7*, 3767. doi: 10.1038/s41598-017-03942-z.
- (32) Galanti, M.; Fanelli, D.; Piazza, F. Conformation-controlled binding kinetics of antibodies. *Sci. Rep.* **2016**, *6*, 18976. doi: 10.1038/srep18976.
- (33) Mack, E. T.; Snyder, P. W.; Perez-Castillejos, R.; Whitesides, G. M. Using covalent dimers of human carbonic anhydrase II to model bivalency in immunoglobulins. *J. Am. Chem. Soc.* **2011**, *133*, 11701-11715.
- (34) Preiner, J.; Kodera, N.; Tang, J.; Ebner, A.; Brameshuber, M.; Blaas, D.; Gelbmann, N.; Gruber, H. J.; Ando, T.; Hinterdorfer, P. IgGs are made for walking on bacterial and viral surfaces. *Nat. Commun.* **2014**, *5*: 4394. doi: 10.1038/ncomms5394.
- (35) Huh, Y. O.; Keating, M. J.; Saffer, H. L.; Jilani, I.; Lerner, S.; Albitar M. Higher levels of surface CD20 expression on circulating lymphocytes compared with bone marrow and lymph nodes in B-cell chronic lymphocytic leukemia. *Am. J. Clin. Pathol.* **2001**, *116*, 437-443.
- (36) Cartron, G.; Watier, H.; Golay, J.; Solal-Celigny, P. From the bench to the bedside: ways to improve rituximab efficacy. *Blood* **2004**, *104*, 2635-2642.
- (37) Ward, E.; Mittereder, N.; Kuta, E.; Sims, G. P.; Bowen, M. A.; Dall'Acqua, W.; Tedder, T.; Kiener, P.; Coyle, A. J.; Wu, H.; Jallal, B.; Herbst, R. A glycoengineered anti-CD19 antibody with potent antibody-dependent cellular cytotoxicity activity *in vitro* and lymphoma growth inhibition *in vivo*. *Br. J. Haematol.* **2011**, *155*, 426-437.
